

1 **Performance Characteristics of the Biograph Vision Quadra PET/CT**
2 **system with long axial field of view using the NEMA NU 2-2018 Standard**

3
4 George A. Prenosil^{1*}, Hasan Sari^{1,2}, Markus Fürstner¹, Ali Afshar-Oromieh¹, Kuangyu Shi¹, Axel
5 Rominger¹ and Michael Hentschel¹

6 *1 Department of Nuclear Medicine, Inselspital, Bern University Hospital, University of Bern, Bern, Switzerland*

7 *2 Advanced Clinical Imaging Technology, Siemens Healthcare AG, Lausanne, Switzerland;*

8 ** Corresponding Address: George A. Prenosil, Department of Nuclear Medicine, Inselspital Bern, 3010 Bern, Switzerland;*

9 *Tel.: +41 31 632 76 51, Fax.: +41 31 632 76 63, e-mail: george.prenosil@insel.ch*

10

11 **Disclaimer:** Hasan Sari is a full-time employee of Siemens Healthcare AG, Switzerland.

12

13 *Word count: 6165*

14

15 **ABSTRACT**

16 **Purpose:** To evaluate the performance of the Biograph Vision Quadra (Siemens Healthineers) PET/CT
17 system. This new system is based on the Siemens Biograph Vision 600, using the same silicon
18 photomultiplier-based detectors with 3.2×3.2×20-mm lutetium-oxoorthosilicate crystals. The Quadra's 32
19 detector rings provide a fourfold larger axial field of view (AFOV) of 106 cm, enabling imaging of major
20 organs in one bed position.

21 **Methods:** Physical performance of the scanner was evaluated according to the National Electrical
22 Manufacturers Association NU 2-2018 standard with additional experiments to characterize energy
23 resolution. Image quality was assessed with foreground to background ratios of 4:1 and 8:1. Additionally,
24 a clinical ¹⁸F-FDG-PET study was reconstructed with varying frame durations. In all experiments, data
25 were acquired using the Quadra's maximum ring distance of 322 crystals (MRD 322), while image
26 reconstructions could only be performed with a maximum ring distance of 85 crystals rings (MRD 85).

27 **Results:** The spatial resolution at full width half maximum in radial, tangential and axial directions were
28 3.3, 3.4 and 3.8 mm respectively. The sensitivity was 83 cps/kBq for MRD 85 and 176 cps/kBq for
29 MRD 322. The NECRs at peak were 1613 kcps for MRD 85 and 2956 kcps for MRD 322, both at
30 27.5 kBq/mL. The respective scatter fractions at peak NECR equaled 36 % and 37 %. The TOF resolution
31 at peak NECR was 228 ps for MRD 85 and 230 ps for MRD 322. Image contrast recovery ranged from
32 69.6% to 86.9 % for 4:1 contrast ratios and from 77.7 % to 92.6 % for 8:1 contrast ratios reconstructed
33 using PSF-TOF with 8 iterations and 5 subsets. Thirty seconds frames provided readable lesion detectability
34 and acceptable noise levels in clinical images.

35 **Conclusions:** The Biograph Vision Quadra PET/CT has similar spatial and time resolution compared to
36 the Biograph Vision 600 but exhibits improved sensitivity and NECR due to its extended AFOV. The
37 reported spatial resolution, time resolution, and sensitivity makes it a competitive new device in the class
38 of PET-scanners with extended AFOV.

39 **Key Words:** Acceptance test, long field of view, total-body, NEMA, digital PET

40

41 INTRODUCTION

42 Over the last decades, positron emission tomography in combination with computed tomography
43 (PET/CT) has consolidated and expanded its role as a standard of care imaging modality in many
44 clinical fields. This growth in usage went hand in hand with technological progress, such as the
45 exploitation of faster scintillators and improved time of flight (TOF) performance (1), extended
46 field of view (FOV) and resolution recovery methods for image reconstruction (2).

47 Recently, digital PET (3,4) replaced bulky photomultiplier tubes (PMTs) with silicon
48 photomultipliers (SiPM), using single-photon avalanche diodes operating in Geiger mode to detect
49 scintillation photons generated from the transfer of energy of annihilation photons in the
50 scintillator. Silicon photomultipliers are not only smaller than PMTs, but also provide a 1000 times
51 larger gain and increased energy resolution (5). Thanks to high amplification, a fast signal, and
52 high light collection, SiPM-based PET systems achieve a time resolution as low as 214 ps (6),
53 compared to the 540 ps of PET systems using PMTs (7,8). When SiPMs are directly coupled to a
54 fast scintillator such as lutetium-oxyorthosilicate, the resulting excellent TOF increases PET
55 sensitivity and reduces noise; in conjunction with small size crystals, the TOF gain provides
56 improved image resolution, improved detectability, and reduced image noise (6,9). The sensitivity
57 gain can be used for the reduction of administered radioactivity dose or alternatively for shortening
58 the acquisition duration (10,11).

59 Current clinical PET/CT systems typically cover an axial FOV (AFOV) of about 15 to 26 cm.
60 As a result, only about 1 % to 3 % of the possible positron/electron annihilation events produce
61 coincidence lines of response (LORs) that are actually detected. Furthermore, in many clinical
62 scenarios, time consuming multiple bed positions must be imaged to cover the relevant portion of
63 the patient. Stretching the FOV by axially spacing out the detector rings increases coverage of the

64 patient body but not the overall sensitivity (12). The viable solution is to increase the number of
65 detector rings at the down side of increased costs (13). The Explorer consortium, United imaging
66 Healthcare Shanghai in collaboration with UC Davis team (14-16) and the University of
67 Pennsylvania (17), and Siemens Healthineers (Erlangen, Germany) (18,19) all developed systems
68 with long AFOVs (LAFOV), covering an axial length spanning from 64 cm to 194 cm. The
69 Biograph Vision Quadra from Siemens Healthineers is a commercially available PET/CT system
70 that combines SiPM detector technology with an optimal (13,15,18) near total-body coverage
71 (106 cm AFOV). Essentially, the Biograph Vision Quadra comprises the equivalent of four axially
72 concatenated PET subsystems of Biograph Vision 600 PET/CT systems, building on proven high
73 spatial resolution and high time resolution technology (6,20).

74 The development of LAFOV PET/CT scanners offers a great opportunity to improve clinical
75 workflow and explore new applications (13,15,18). The high sensitivity allows for very low dose
76 or very fast scans (21) (with higher throughput, better patient comfort, less motion artifacts) in
77 today's clinical routine. In terms of new applications, high sensitivity and simultaneous coverage
78 of multiple organs enables, among other new research topics, low counts imaging (monoclonal
79 antibodies imaging or cell tracking), multi-organ interaction studies (brain-guts, brain-spine, and
80 so on), parametric imaging and pharmaceutical kinetics investigation.

81 Even though human imaging studies had been performed earlier on a total-body PET (16,21),
82 comparable standardized performance data of the uEXPLORER (United imaging Healthcare,
83 Shanghai, PR China) with an AFOV of 194 cm (22) and the PennPET Explorer with an AFOV of
84 64 cm (17) were published only very recently.

85 Published first in 1994 (23) by the National Electrical Manufacturers Association (NEMA), the
86 NEMA NU 2 standards quickly became the accepted set of measurements for benchmarking
87 commercial PET/CT systems. The aim of this study was therefore to evaluate the performance of

88 the new commercially available LAFOV Biograph Vision Quadra PET/CT system according to
89 the latest NEMA NU 2-2018 standard (24). The measurements included spatial resolution, scatter
90 fraction, noise equivalent count rate (NECR), sensitivity, correction accuracies, PET and CT co-
91 registration accuracy, image quality, and TOF resolution. Furthermore, energy resolution of the
92 scanner is reported and clinical images from one of the initial patient studies are illustrated.

93 **MATERIALS AND METHODS**

94 **Biograph Vision Quadra PET/CT System Specifications**

95 The Biograph Vision Quadra uses the technology previously developed for the Biograph
96 Vision 600 PET/CT system (6,20). The lutetium-oxoorthosilicate crystals of are directly coupled
97 to a SiPM array with 16 output channels. Eight mini-blocks form a detector block, with two
98 adjacent detector blocks always sharing a common electronic unit. The Biograph Vision Quadra
99 has four times the number of detector rings found in the Biograph Vision, with a total axial span
100 of 320 crystals. This arrangement gives the Biograph Vision Quadra an AFOV of 106 cm, versus
101 26.3 cm as compared to the Biograph Vision 600 (7). Table 1 details more system specifications.

102 The Biograph Vision Quadra records all possible LORs using its maximum full ring difference
103 (MRD) of 322 crystal rings (MRD 322), with an acceptance angle of 52° . In this first version of
104 the reconstruction software (VR10), also named High Sensitivity mode, images are reconstructed
105 with LORs spanning a MRD of 85 crystal rings (MRD 85). This MRD is comparable to the
106 Biograph Vision's MRD of 79 (7), corresponding to an acceptance angle for axial LOR of about
107 18° . The MRD metric refers to the number of crystals in the LOR's axial extend and includes the
108 gaps between blocks. In MRD 85 mode, the Vision Quadra does not use all the possible LORs
109 between scintillating crystals for image reconstruction. In this work, all data were acquired using
110 MRD 322, while image reconstructions were performed using only MRD 85. For experiments

111 where no image reconstruction was required, results for MRD 85 and MRD 322 are reported side
112 by side. Although currently unsuitable for clinical application, MRD 322 measurements are still
113 useful in a scientific context.

114 **Performance Measurements**

115 The performance of the Biograph Vision Quadra PET/CT system installed at the nuclear
116 medicine department of the Inselspital Bern was benchmarked according to the NEMA NU 2-2018
117 standard (24). Additionally, we measured the Biograph Vision Quadra's energy resolution, which
118 is not part of the NEMA 2018 measurement set. Data were analyzed using the NEMA tools
119 software (Siemens Healthineers).

120 In addition, PET images from a human study are presented to illustrate image quality together
121 with some initial quantification results. All PET images in this work were reconstructed into a
122 matrix of $440 \times 440 \times 645$ with an isotropic voxel spacing of 1.65 mm. This is also the innate
123 sampling resolution of the Quadra PET/CT.

124 ***Spatial Resolution***, Spatial resolution was measured at six different positions (Table 2,
125 Supplemental Fig. 1) using a point source with 0.25 mm diameter containing 393 kBq ^{22}Na (Eckert
126 und Ziegler).

127 After acquiring at least 4×10^6 true counts for every position, images were reconstructed in
128 MRD 85, without the use of a post reconstruction filter, and with direct inversion Fourier transform
129 back-projection (3D-TOFDIFT), an analytical back-projection reconstruction method (18).
130 Corrections were applied for detector normalization, dead time, radial-arc-correction decay and
131 randoms, but no scatter or attenuation correction was employed.

132 Resolution was reported as the full width at half-maximum (FWHM) and full width at tenth
133 maximum (FWTM) of the point source's spread in radial, tangential and axial direction. For each
134 direction, average values over the two axial positions were calculated.

135 **Count Rates: Trues, Randoms, Scatters and Noise Equivalent Counts,** For count rate
136 measurements, we used a solid polyethylene cylinder with an outside diameter of 20.3 cm and
137 70 cm length. A 3 mm wide and 70 cm long polyethylene capillary was filled with 894 MBq ^{18}F
138 and inserted in a 6.4 mm wide hole running parallel to the central axis of the cylinder at radial
139 offset of 45 mm.

140 The cylinder phantom was placed onto the patient table in the center of the FOV and axially
141 aligned with the PET/CT system. The line source insert was positioned close to the patient table,
142 and foam blocks were used to elevate the phantom above the table to an axially aligned position.
143 Data acquisitions in list-mode were performed over the course of 700 min. However, the NEMA
144 NU 2 criteria of waiting until true event losses are less than 1.0 % could not be achieved due to the
145 intrinsic radioactivity of lutetium-oxoorthosilicate. Therefore, a different methodology had to be
146 used as described in reference (25): Count rates were measured using delayed coincidence
147 windows, and the scatter fraction was calculated as a function of count rate.

148 Every 20 min data were acquired for 240 s, and the acquisitions were binned into 35 individual
149 sinograms of equal duration. Data were not corrected for variations in detector sensitivity, randoms,
150 scatter, dead time, or attenuation effects.

151 Rates of total, true, scatter and noise equivalent counts (NEC) were calculated as specified by
152 Section 4 of the NEMA NU 2-2018 protocol. Prompt and random sinograms were generated for
153 each acquisition and each slice. Because of the Quadra's extended AFOV, only slices located
154 within the central 65 cm of the AFOV were used for histogram generation.

155 **Sensitivity,** For sensitivity measurements, we used the same 70 cm long polyethylene capillary
156 as described above and filled it over a total length of 68 cm with an aqueous solution of
157 4.56 MBq ^{18}F . The line source was surrounded by five concentric aluminum sleeves of matching
158 length and with known radiation attenuation. The setup was bedded on foam holders with

159 negligible attenuation. One sensitivity measurement series was performed with the capillary axially
160 aligned at the center of the AFOV and the other series was performed with a 10 cm radial offset
161 added to the first placement. The supports for the capillary stayed outside the FOV. By measuring
162 the count rate while consecutively removing sleeves, we extrapolated the attenuation-free count
163 rate, e.g. the count rate of the naked line source (26). Data were acquired for 300 s for each sleeve.

164 **Accuracy: Correction for Count Losses and Randoms**, Data acquired for count rate
165 measurements were used to estimate the accuracy of the correction of count losses due to detector
166 dead time and due to random counts (randoms). Corrections for randoms, scatter, dead time, and
167 attenuation were applied. For attenuation correction, a low dose CT of the phantom was acquired
168 with 120 keV tube voltage, 80 mAs tube current and 0.8 pitch. The CT image was reconstructed
169 into a 512×512 matrix. Scatter was corrected for as described by Watson *et al.* (27).

170 The PET image was reconstructed from MRD 85 data using OSEM-TOF with 4 iterations, 5
171 subsets, and 2 mm Gaussian post-reconstruction filtering.

172 **Image Quality, Accuracy of Corrections**, A NEMA International Electrotechnical Commission
173 (IEC) body phantom (28) of 180 mm interior length was used for assessing image quality and the
174 accuracy of attenuation and scatter corrections. The gravimetrically determined volume of the
175 background compartment was 9742 mL, and the fillable six spheres had internal diameters of 10,
176 13, 17, 22, 28, and 37 mm. The central lung insert filled with polystyrene beads was void of any
177 activity.

178 Background activity concentration was 5.3 kBq/mL ¹⁸F at the start of image acquisition,
179 constituting our low activity concentration benchmark. A first measurement was taken with all
180 spheres filled with a concentration of four times that of the background as stated in the NEMA
181 NU 2-2018 protocol (24). A second measurement was taken with a concentration of eight times
182 that of the background. The phantom was axially aligned with the spheres positioned around the

183 center of the FOV. The cylindrical scatter phantom was positioned adjacent to the sphere-
184 containing phantom, and its line source was filled with 100 MBq ^{18}F at the start of the acquisition.

185 A single bed position was acquired for 30 min in list-mode. Data were corrected for decay,
186 normalization, scatter, randoms and attenuation. The required attenuation CT was acquired before
187 the PET measurements as described above. Images were reconstructed in MRD 85 using OSEM-
188 TOF and PSF-TOF with 8 iterations, 5 subsets. Both reconstructions were also performed using 4
189 iterations and 5 subsets. No post-reconstruction filtering was applied. Activity spill-in into the cold
190 lung insert was used to calculate an average residual error.

191 ***Time-Of-Flight and Energy Resolution,*** To measure the positional uncertainty of the
192 coincidence event localization, we used the same CT and PET data as previously acquired for the
193 NECR experiment, without corrections applied.

194 To determine the position of the line source, the first frame with activity below the peak NECR
195 was reconstructed in MRD 85 using OSEM with 10 iterations and 5 subsets with scatter, random
196 and attenuation correction, but without decay correction. The method to calculate TOF resolution
197 is described in Section 8 of the NEMA NU-2 2018 standard and in Wang, *et al.* (29).

198 For measuring the energy resolution of the scanner, we used the same data but without any
199 corrections applied. This measurement is not part of the NEMA NU 2-2018 standard, but it is based
200 on the same method as for the TOF resolution, and is described in reference (30). An image
201 reconstruction was performed for determining the line source centroid with scatter, random and
202 attenuation correction, but without decay correction. Trues were assumed to be within a
203 perpendicular distance of +/-20 mm of line source data and thus counts at +/-20 mm were assumed
204 to come from scatter, randoms, and background. For each crystal, an energy histogram was
205 generated using all events within a distance of -20 and +20 mm. The weighted combination of
206 counts at -20 mm and +20 mm, as done in NEMA count-rate studies, was used to estimate the

207 background (scatter and randoms). All crystal peaks were aligned and added in a common energy
208 histogram (Supplemental Fig. 2). The energy resolution was defined as the FWHM of the energy
209 spectrum so obtained. For comparison, the energy resolution was also measured using a more
210 conventional method, by placing a 19 cm long line source containing 19.19 MBq ^{68}Ge without a
211 scattering medium at the center of the FOV.

212 ***PET-CT Co-Registration Accuracy***, Co-registration accuracy between the PET and the CT
213 image was measured with a vial of 13.3 mm diameter and conical bottom and filled with an aqueous
214 solution of 0.2 mL 370 MBq ^{18}F and 1 mL CT contrast (Ultravist 370, Bayer Vital) according to
215 the NEMA NU 2-2018 document (24). CT images were reconstructed into a 512×512 matrix and
216 slice thickness of 0.6 mm, and PET images were reconstructed using OSEM-TOF with 10 iterations
217 and 5 subsets, without attenuation correction or post-reconstruction filtering.

218 ***Human Studies***, An oncologic female patient (age: 81 y, height: 160 cm, weight: 57 kg)
219 participating in a clinical study (31) was scanned 60 min after administration of 191 MBq ^{18}F -
220 FDG. A single bed position was acquired for 10 min. Eight images were reconstructed by binning
221 the list-mode data into 10 min, 6 min, 4 min, 3 min, 2 min, 1 min, 30 s, and 15 s frames. Images
222 were reconstructed using TOF-PSF with 4 iterations, 5 subsets, and 2 mm FWHM Gaussian post-
223 filter.

224 An isocontour threshold of 40 % delineated the VOI of a FDG avid lesion in the 10 min frame,
225 and a sphere VOI with a diameter of 5.1 cm was placed in the center of the liver in the same frame.
226 Both VOIs were then copied into the remaining frames. Standard uptake values (SUV) and
227 coefficient-of-variation (CV) values were computed for each VOI in every frame.

228 The human study (31) had been approved by the regional ethics committee, and the patient had
229 signed an informed consent form.

230

231 **RESULTS**

232 **Spatial Resolution**

233 Table 2 reports the FWHM and FWTM values measured for the six different positions in
234 MRD 85 mode.

235 **Count Rates: Trues, Randoms, Scatters and Noise Equivalent Counts**

236 Fig. 1 shows count rate plots for trues, randoms, scatter and NEC measured at MRD 85 and
237 MRD 322, as well as for scatter fractions at peak NECR. Table 3 summarizes the count rate
238 findings. As all events were recorded regardless of the MRD setting, the peak NECR of 1613 kcps
239 for MRD 85 and of 2956 kcps for MRD 322 were both observed at 27.49 kBq/mL.

240 **Sensitivity**

241 Table 4 reports total sensitivity values measured for the Biograph Vision Quadra for both MRD
242 modes. The average system sensitivities are 83.4 cps/kBq for MRD 85 and 176.0 cps/kBq for
243 MRD 322.

244 Fig. 2 exhibits the axial sensitivity profiles. While MRD 85 provides for homogeneous
245 sensitivity of around 200 cps/MBq over the measured AFOV, MRD 322 shows a peak of
246 549 cps/MBq in the middle of the AFOV. As expected, the MRD 85 mode gives the Biograph
247 Vision Quadra a flat sensitivity similar to the Biograph Vision 600's peak sensitivity (6). In
248 MRD 322 mode, the axial peak sensitivity of the Biograph Vision Quadra is 2.75 times higher than
249 the axial peak sensitivity found in the Biograph Vision 600 (6).

250 **Accuracy: Correction for Count Losses and Randoms**

251 Accuracy measurements were obtained from the difference between expected and measured
252 activity concentration on the PET data as previously acquired for the NECR in MRD 85. Fig. 3
253 shows the minimum and maximum error in the PET image plotted against activity concentration.
254 The count rate errors were below 5 % (maximum) and 10 % (minimum), up to the peak NECR;
255 after this discontinuity, both error curves increased their negative slopes by a factor of 20.

256 **Image Quality, Accuracy of Corrections**

257 Table 5 reports the contrast recovery, relative background variability, and the lung residual error
258 for images reconstructed with OSEM-TOF for the two sphere-to-background ratios examined, and
259 Table 6 reports the same for images reconstructed with PSF-TOF.

260 **Time-Of-flight and Energy Resolution**

261 The TOF resolution at peak NECR was 228 ps for MRD 85 and 230 ps for MRD 322. At a low
262 (background) activity concentration of 5.3 kBq/mL, the TOF resolutions were 225 ps and 228 ps
263 respectively (Table 3). Fig. 4A shows the time resolution over the whole activity range.

264 Calculated energy resolution in MRD 85 mode was 10.1 % at peak NECR and 9.8 % at
265 5.30 kBq/mL (Fig. 4B). When measured using the ⁶⁸Ge line source, energy resolution was with
266 8.9 % at peak NECR slightly better due to the absence of scattered photons. This value was almost
267 identical to the 9.0 % published for the Biograph Vision 600 (20).

268 **PET-CT Co-Registration Accuracy**

269 The maximum co-registration error was +1.38 mm. Supplemental Table 1 reports the six
270 individual co-registration measurements.

271 **Human Studies**

272 Excellent image quality was observed in ^{18}F -FDG images (Fig. 5) reconstructed with longer
273 frame durations, with slightly higher noise seen in frames reconstructed with 30 s and 15 s. The
274 evaluated lesion had a diameter of 1.58 cm and was detectable in all eight frames. However, image
275 noise started to become a problem in the 15 s frame with a lesion CV of 0.52 and a liver CV of
276 0.22.

277 Fig. 6A shows the SUVs within the tumor and liver for each frame duration. The CV log-log
278 plots show the expected power law in respect to frame duration (Fig. 6B).

279 **DISCUSSION**

280 No significant difference in spatial resolution was found between our data from the Biograph
281 Vision Quadra and previously published data from the Biograph Vision (6) (Paired Wilcoxon
282 signed-ranked test). This is to be expected since crystal and detector size, geometry, and readout
283 are the same in both scanners.

284 The NEMA NECRs at peak were 1641 kcps for MRD 85 and 3018 kcps for MRD 322, with
285 both peaks occurring at 28.3 kBq/mL. The NECR curve (Fig. 1) has a discontinuity and drops down
286 after the peak; this happens when count rate reaches the maximum total events throughput
287 supported by the hardware (19), which is around 129 Mcps. We should note that this occurs even
288 far above actual clinical (31) or even high-count regimes (20).

289 The NEMA sensitivities were 83.4 cps/kBq and 176 cps/kBq for MRD 85 and MRD 322,
290 respectively. As a comparison, the Biograph Vision 600 has a sensitivity at the center of
291 16.4 cps/kBq and a peak NECR of 306 kcps: The Biograph Quadra provides a NEMA sensitivity
292 which is about 5 times that of the Biograph Vision in MRD 85 and about 10 times in MRD 322
293 mode (6). In fact, the NEMA sensitivity of the Biograph Quadra at in MRD 322 is at par with the

294 uEXPLORER (22), which is not surprising, given the size of the source and the two scanner's
295 similar acceptance angle for axial LORs.

296 The TOF resolution was 225 ps for MRD 85 and 227 ps for MRD 322. The measured time
297 resolution on the Quadra was slightly worse than the published value for Vision 600 (6), possibly
298 due to non-uniformity of detector and signal sync over a larger number detectors and electronic
299 modules and a not yet optimized time alignment method. In fact, both time and energy resolution
300 of the scanner are stable with count rate, exhibiting a change of only 2-3 % over the whole count
301 rate range.

302 This high time resolution functions as an additional equivalent counts amplifier, which allows
303 the effective sensitivity to increase by a TOF gain factor of about $D/(\Delta t \times c/2)$, according to the
304 standard TOF gain model (where D is size of the patient, Δt is the time resolution, and c is the
305 speed of light). Better time-of-flight-resolution translates in lower image noise, at equal number of
306 counts, and higher robustness of the reconstruction (10,32,33), as compared with PET scanners
307 with similar NEMA sensitivity but poorer time resolution.

308 Because we followed the NEMA NU 2-2018 protocol and not the NEMA NU 2-2012, only the
309 results for the four smallest spheres are comparable with those published for the Biograph
310 Vision 600 (6). The contrast was comparable to those of the four spheres reconstructed with PSF-
311 TOF, but background variability was around 2.5 times lower for the Quadra (6). This can be
312 explained by the Quadra's five times higher sensitivity at equal spatial resolution. As previously
313 shown for the Biograph Vision 600 (6), Gibbs artefacts increase contrast in the smallest sphere.
314 This is a well-known characteristic of resolution recovery or PSF reconstruction (34). All images
315 were reconstructed with the MRD 85 mode's low sensitivity, leading to a lower than possible
316 contrast to noise ratio. In a future software update, the Ultra High Sensitivity mode will be

317 available, with MRD 322, where all LORs spanning the full AFOV will be used in image
318 reconstruction. However, the impact of oblique LORs on image quality remains to be examined.

319 From the patient images, we expect that clinical acquisitions below two minutes can provide
320 acceptable image quality when using the Quadra. Besides exploiting the increased sensitivity of
321 the system for reductions in injected dose, delayed or prolonged imaging regimes are also
322 conceivable (31). Additionally, the Quadra is suited for temporally and spatially well-resolved
323 dynamic studies that cover the entire upper body.

324 **CONCLUSION**

325 The Biograph Vision Quadra PET/CT has similar spatial and time resolution compared to the
326 PET/CT Biograph Vision 600 but exhibits improved sensitivity and NECR (5x or 10x, depending
327 on MRD mode) due to the extended AFOV. The high time resolution allows for state-of-the-art
328 noise-reducing TOF reconstructions. The combination of high spatial resolution, high time
329 resolution, and very high sensitivity makes the Quadra a high performance new device in the class
330 of total-body PET scanners.

331 **ACKNOWLEDGMENTS**

332 Thank goes to Kevin Lohmann and Colin Ward, for assistance with the PET measurements. We
333 thank Maurizio Conti and Bernard Bendriem for their useful discussions.

334 **DISCLOSURE**

335 Hasan Sari is a full-time employee of Siemens Healthcare AG, Switzerland. No other potential
336 conflicts of interest relevant to this article exist.

337 **KEY POINTS**

338 QUESTION: What are the performance characteristics of the new Biograph Vision Quadra
339 (Siemens Healthineers) total-body PET/CT system according to the NEMA NU 2-2018 standard?

340 PERTINENT FINDINGS: The Biograph Vision Quadra has similar spatial resolution but, due
341 to its extended AFOV, has a five to ten times higher NECR and an up to 2.75 times higher peak
342 sensitivity than the Biograph Vision 600.

343 IMPLICATION FOR PATIENT CARE: The Biograph Vision Quadra's increased sensitivity
344 allows for total body imaging with reduced injected dose or reduced acquisition duration, and
345 dynamic studies can be conducted with high spatial and high temporal resolution.

346

347 **REFERENCES**

- 348 1. Surti S, Kuhn A, Werner ME, Perkins AE, Kolthammer J, Karp JS. Performance of Philips
349 Gemini TF PET/CT scanner with special consideration for Its time-of-flight imaging capabilities. *J*
350 *Nucl Med.* 2007;48:471-480.
- 351
- 352 2. Jakoby BW, Bercier Y, Watson CC, Bendriem B, Townsend DW. Performance characteristics
353 of a new LSO PET/CT scanner with extended axial field-of-view and PSF reconstruction. *IEEE*
354 *Trans Nucl Sci.* 2009;56:633-639.
- 355
- 356 3. Koopman D, Groot Koerkamp M, Jager PL, et al. Digital PET compliance to EARL accreditation
357 specifications. *EJNMMI Phys.* 2017;4:9.
- 358
- 359 4. Nguyen NC, Vercher-Conejero JL, Sattar A, et al. Image quality and diagnostic performance
360 of a digital PET prototype in patients with oncologic diseases: initial experience and comparison
361 with analog PET. *J Nucl Med.* 2015;56:1378-1385.
- 362
- 363 5. Bisogni MG, Del Guerra A, Belcari N. Medical applications of silicon photomultipliers. *Nuclear*
364 *Instruments and Methods in Physics Research Section A: Accelerators, Spectrometers, Detectors*
365 *and Associated Equipment.* 2019;926:118-128.
- 366
- 367 6. van Sluis J, de Jong J, Schaar J, et al. Performance characteristics of the digital Biograph
368 Vision PET/CT system. *J Nucl Med.* 2019;60:1031-1036.
- 369
- 370 7. Carlier T, Ferrer L, Conti M, et al. From a PMT-based to a SiPM-based PET system: a study
371 to define matched acquisition/reconstruction parameters and NEMA performance of the Biograph
372 Vision 450. *EJNMMI Phys.* 2020;7:55-55.

- 373
- 374 **8.** Gnesin S, Kieffer C, Zeimpekis K, et al. Phantom-based image quality assessment of clinical
375 18F-FDG protocols in digital PET/CT and comparison to conventional PMT-based PET/CT.
376 *EJNMMI Phys.* 2020;7:1.
- 377
- 378 **9.** Alberts I, Prenosil G, Sachpekidis C, et al. Digital versus analogue PET in [68Ga]Ga-PSMA-
379 11 PET/CT for recurrent prostate cancer: a matched-pair comparison. *Eur J Nucl Med Mol*
380 *Imaging.* 2020;47:614-623.
- 381
- 382 **10.** Surti S, Viswanath V, Daube-Witherspoon ME, Conti M, Casey ME, Karp JS. Benefit of
383 improved performance with state-of-the art digital PET/CT for lesion detection in oncology. *J Nucl*
384 *Med.* 2020;61:1684-1690.
- 385
- 386 **11.** van Sluis J, Boellaard R, Dierckx RAJO, Stormezand GN, Glaudemans AWJM, Noordzij W.
387 Image quality and activity optimization in oncologic 18F-FDG PET using the digital Biograph Vision
388 PET/CT system. *J Nucl Med.* 2020;61:764-771.
- 389
- 390 **12.** Zein S, Karakatsanis N, Issa M, Haj - Ali A, Nehmeh S. Physical performance of a long axial
391 field of view PET scanner prototype with sparser rings configuration: a Monte Carlo simulation
392 study. *Med Phys.* 2020;47:1949-1957.
- 393
- 394 **13.** Cherry SR, Jones T, Karp JS, Qi J, Moses WW, Badawi RD. Total-body PET: maximizing
395 sensitivity to create new opportunities for clinical research and patient care. *J Nucl Med.*
396 2018;59:3-12.
- 397

- 398 **14.** Badawi RD, Shi H, Hu P, et al. First human imaging studies with the EXPLORER total-body
399 PET scanner*. *J Nucl Med.* 2019;60:299-303.
400
- 401 **15.** Surti S, Pantel AR, Karp JS. Total body PET: why, how, what for? *IEEE Trans Radiat Plasma*
402 *Med Sci.* 2020;4:283-292.
403
- 404 **16.** Zhang J, Maniawski P, Knopp MV. Performance evaluation of the next generation solid-state
405 digital photon counting PET/CT system. *EJNMMI Res.* 2018;8:97.
406
- 407 **17.** Karp JS, Viswanath V, Geagan MJ, et al. PennPET Explorer: design and preliminary
408 performance of a whole-body imager. *J Nucl Med.* 2020;61:136-143.
409
- 410 **18.** Conti M, Aykac M, Bal H, et al. Simulation and first measurements on a prototype ultra-long
411 FOV PET/CT scanner. Paper presented at: EANM'20, 2020; Vienna.
412
- 413 **19.** Siegel S, Aykac M, Bal H, et al. Preliminary performance of a prototype, one-meter long PET
414 tomograph. Paper presented at: 2020 IEEE Nuclear Science Symposium & Medical Imaging
415 Conference; 5. November, 2020, 2020; Virtual.
416
- 417 **20.** Reddin JS, Scheuermann JS, Bharkhada D, et al. Performance evaluation of the SiPM-based
418 Siemens Biograph Vision PET/CT system. Paper presented at: 2018 IEEE Nuclear Science
419 Symposium and Medical Imaging Conference Proceedings (NSS/MIC); 10-17 Nov. 2018, 2018.
420
- 421 **21.** Zhang Y-Q, Hu P-C, Wu R-Z, et al. The image quality, lesion detectability, and acquisition time
422 of ¹⁸F-FDG total-body PET/CT in oncological patients. *Eur J Nucl Med Mol Imaging.*
423 2020;47:2507-2515.

424

425 **22.** Spencer BA, Berg E, Schmall JP, et al. Performance evaluation of the uEXPLORER Total-
426 body PET/CT scanner based on NEMA NU 2-2018 with additional tests to characterize long axial
427 field-of-view PET scanners. *J Nucl Med.* 2020;Epub ahead of print.

428

429 **23.** NEMA standards publication NU 2-1994: performance measurements of positron emission
430 tomographs. In: National Electrical Manufacturers Association, ed. 12 ed. Washington DC:
431 National Electrical Manufacturers Association; 1994.

432

433 **24.** NEMA standards publication NU 2-2018: performance measurements of positron emission
434 tomographs (PET). In: National Electrical Manufacturers Association, ed. 18 ed. 1300 N. 17th
435 Street, Suite 900, Rosslyn, VA 22209: National Electrical Manufacturers Association; 2018:41.

436

437 **25.** Watson CC, Casey ME, Eriksson L, Mulnix T, Adams D, Bendriem B. NEMA NU 2 performance
438 tests for scanners with intrinsic radioactivity. *J Nucl Med.* 2004;45:822-826.

439

440 **26.** Bailey DL, Jones T, Spinks TJ. A method for measuring the absolute sensitivity of positron
441 emission tomographic scanners. *Eur J Nucl Med.* 1991;18:374-379.

442

443 **27.** Watson CC. New, faster, image-based scatter correction for 3D PET. *IEEE Trans Nucl Sci.*
444 2000;47:1587-1594.

445

446 **28.** IEC Standard 61675-1: radionuclide imaging devices - Characteristics and test conditions -
447 Part 1: Positron emission tomographs Geneva, Switzerland: International Electrotechnical
448 Commission 1998:36.

449

450 **29.** Wang G-C, Li X, Niu X, et al. PET timing performance measurement method using NEMA NEC
451 phantom. *IEEE Trans Nucl Sci.* 2016;63:1335-1342.

452
453 **30.** Bharkhada D, Rothfuss H, Conti M. A new method to calculate energy resolution based upon
454 NEC phantom. Paper presented at: 2017 IEEE Nuclear Science Symposium and Medical Imaging
455 Conference (NSS/MIC); 21-28 Oct. 2017, 2017.

456
457 **31.** Alberts I, Hünernmund JN, Prenosil G, et al. Clinical performance of long axial field of view
458 PET/CT: a head-to-head intra-individual comparison of the Biograph Vision Quadra with the
459 Biograph Vision PET/CT. *Eur J Nucl Med Mol Imaging.* 2021; Online ahead of print.

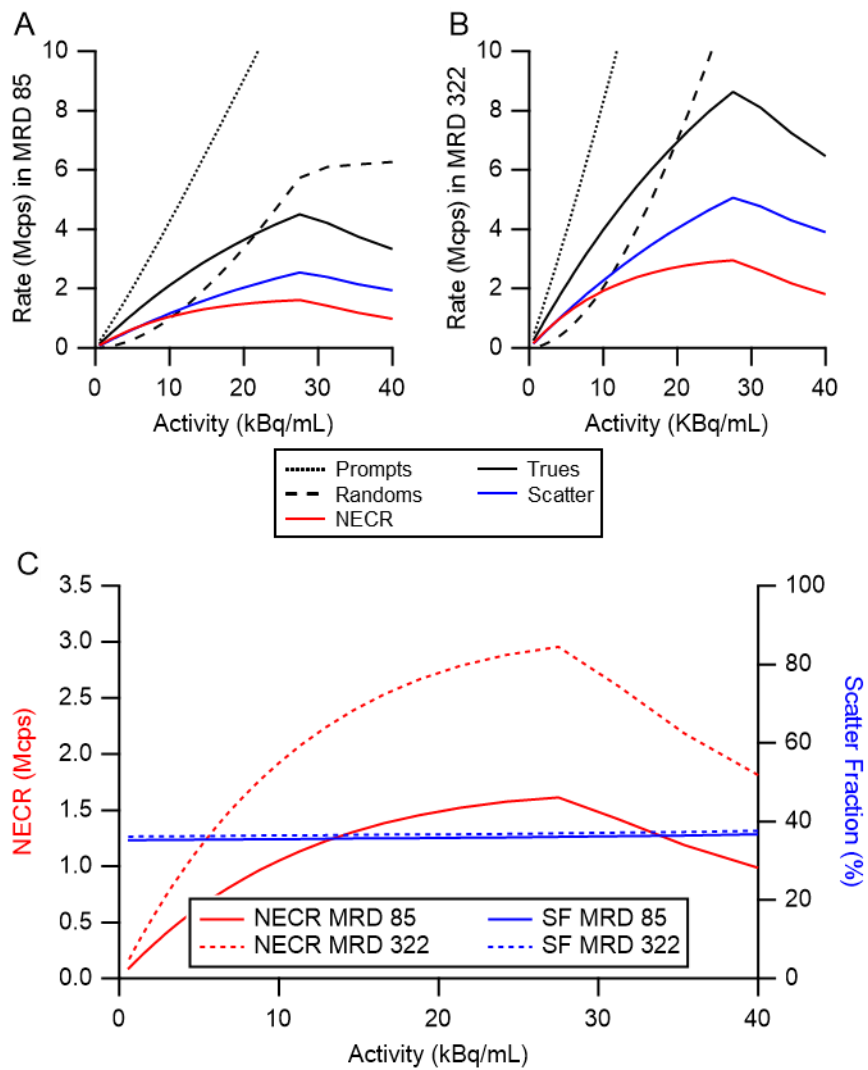
460
461 **32.** Conti M. Focus on time-of-flight PET: the benefits of improved time resolution. *Eur J Nucl Med*
462 *Mol Imaging.* 2011;38:1147-1157.

463
464 **33.** Conti M, Bendriem B. The new opportunities for high time resolution clinical TOF PET. *Clin*
465 *Transl Imaging.* 2019;7:139-147.

466
467 **34.** Rahmim A, Qi J, Sossi V. Resolution modeling in PET imaging: theory, practice, benefits, and
468 pitfalls. *Med Phys.* 2013;40:15.

469
470

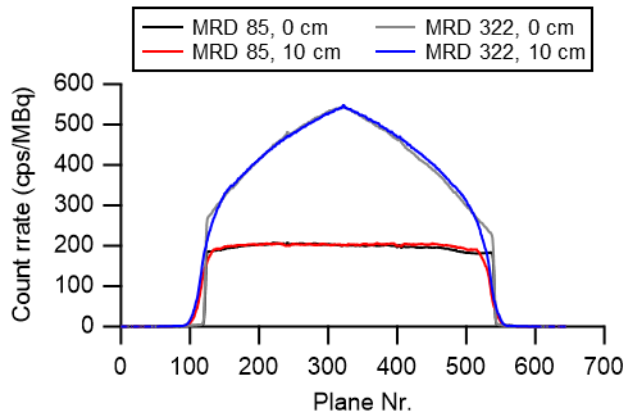
471 **Figure legends**



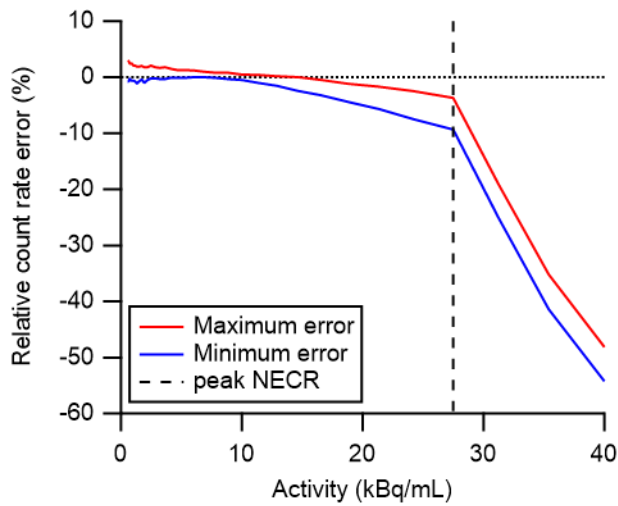
472

473 **FIGURE 1:** Plots of prompts, randoms, trues, scatter and NEC rates for MRD 85 (A), and

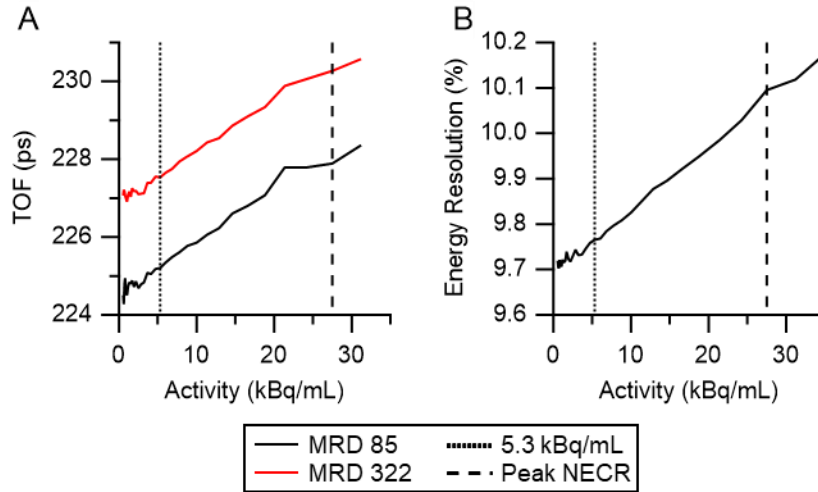
474 MRD 322 (B). (C) NECR and scatter fractions (SF)



475
 476 **FIGURE 2:** Axial sensitivity profiles for the 0 and 10 cm radial offset positions and for both
 477 MRD modes



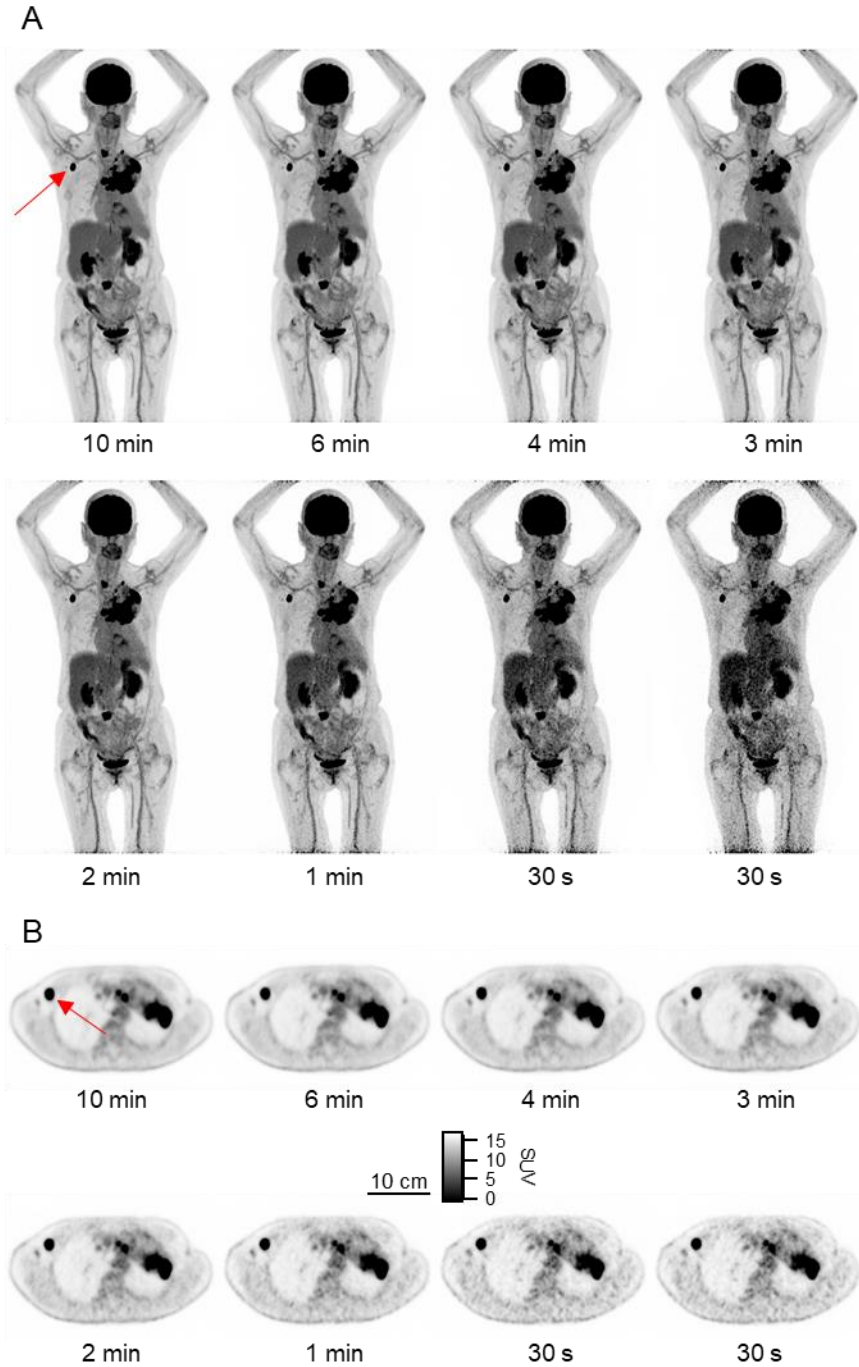
478
 479 **FIGURE 3:** Maximum and minimum relative count rate error in MRD 85 vs. activity
 480 concentration; dashed line highlights values at peak NECR



481

482 **FIGURE 4:** TOF (A) and energy resolution (B) as functions of activity concentration with low

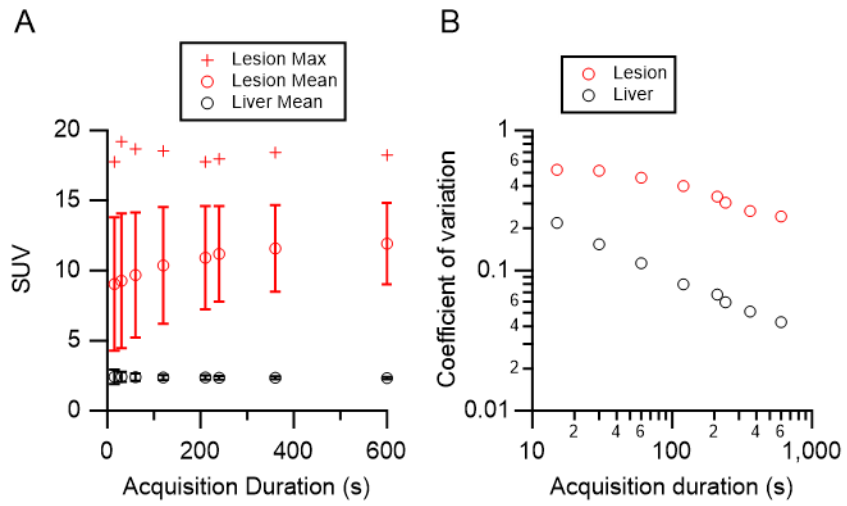
483 and peak NECR activity concentration marked with dashed lines.



484

485 **FIGURE 5:** (A) Maximum intensity projection images of an oncologic patient, reconstructed

486 with different frame durations. (B) Axial PET images containing the reported lesion (red arrows).



487

488 **FIGURE 6:** Tumor and liver SUVs (A) and CV values (B) of the oncologic patient. Mean
 489 values are reported with \pm standard deviation.

490

491 **Tables**

492 **Table 1:** Biograph Vision Quadra system specifications

Crystal size	3.2×3.2×20 mm	SiPM array size	16×16 mm
Crystals per SiPM (mini-block)	5×5	Mini-blocks per detector block	2×4
Detector blocks per ring	38	Detector rings	32
Detector ring diameter	82 cm	Image plane spacing	1.65 mm
Energy window	[435 keV, 585 keV]	Coincidence time window	4.7 ns
PET Axial FOV	106 cm	PET Transaxial FOV	78 cm
CT model	Siemens Definition Edge	CT Generator power	100 kW
CT slices	128	CT minimal slice spacing	0.5 mm
Bore length with CT	230 cm	Total system length	611 cm
Maximal patient weight	227 kg	System weight	5934 kg
Cooling water temperature	[4° C, 12° C]	Operating room temperature	[18° C, 28° C]

493

494 **Table 2:** Spatial resolution in MRD 85 mode

Axial Position (cm)	Radial Position (cm)	FWHM (mm)			FWTM (mm)		
		Radial	Tangential	Axial	Radial	Tangential	Axial
13.3 (1/8 of FOV)	1	3.19	3.58	3.78	6.49	7.15	7.63
13.3 (1/8 of FOV)	10	4.38	3.47	3.84	8.22	6.88	7.74
13.3 (1/8 of FOV)	20	5.82	3.12	4.21	10.71	6.25	8.87
53.0 (1/2 of FOV)	1	3.35	3.31	3.77	6.47	6.33	7.62
53.0 (1/2 of FOV)	10	4.38	3.53	3.90	8.19	6.81	7.80
53.0 (1/2 of FOV)	20	5.84	3.33	4.27	10.82	6.24	9.06
average 1/2 and 1/8	1	3.27	3.44	3.77	6.48	6.74	7.63
average 1/2 and 1/8	10	4.38	3.50	3.87	8.20	6.85	7.77
average 1/2 and 1/8	20	5.83	3.22	4.24	10.77	6.25	8.96

495

496

497 **Table 3:** Count rates, TOF resolution, energy resolution * 100% = 511 keV

Parameter	MRD 85	MRD 322
Peak NECR (kcps @ kBq/mL)	1613 @ 27.49	2956 @ 27.49
Peak true rate (kcps @ kBq/mL)	4501 @ 27.49	8633 @ 27.49
Scatter Fraction @ peak NECR (%)	36	37
TOF resolution @ peak NECR (ps)	228	230
TOF resolution @ 5.3 kBq/mL (ps)	225	228

498

499 **Table 4:** Sensitivity.

	MRD 85	MRD 322
Radial Offset (cm)	Sensitivity (cps/kBq)	Sensitivity (cps/kBq)
0	82.6	175.3
10	84.1	176.7
0 and 10 average	83.4	176.0

500

501

502 **Table 5:** Image quality measurements reconstructed with (A) OSEM-TOF, 8 iterations, 5
 503 subsets and (B) OSEM-TOF, 4 iterations, 5 subsets.

504 (A)

OSEM-TOF 8i5s	4 : 1 Sphere-to-background ratio		8 : 1 Sphere-to-background ratio	
Sphere diameter	Contrast recovery (%)	Background variability (%)	Contrast recovery (%)	Background variability (%)
10	60.11	3.19	64.07	2.73
13	64.52	2.58	70.88	2.37
17	74.33	1.87	82.60	1.85
22	78.02	1.52	84.45	1.41
28	82.83	1.27	87.88	1.01
37	85.23	0.99	91.05	0.87
Average lung residual Error (%)	2.41		2.55	

505

506 (B)

OSEM-TOF 4i5s	4 : 1 Sphere-to-background ratio		8 : 1 Sphere-to-background ratio	
Sphere diameter	Contrast recovery (%)	Background variability (%)	Contrast recovery (%)	Background variability (%)
10	56.35	2.46	61.95	2.14
13	61.52	2.04	68.99	1.88
17	72.26	1.54	80.94	1.51
22	76.33	1.28	83.09	1.2
28	81.35	1.1	86.69	0.91
37	84.24	0.9	90.16	0.81
Average lung residual Error (%)	4.89		5.13	

507

508 **Table 6:** Image quality measurements reconstructed with (A) PSF-TOF, 8 iterations, 5 subsets
 509 and (B) PSF-TOF, 4 iterations, 5 subsets.

510 (A)

PSF-TOF 8i5s	4 : 1 Sphere-to-background ratio		8 : 1 Sphere-to-background ratio	
	Contrast recovery (%)	Background variability (%)	Contrast recovery (%)	Background variability (%)
10	74.44	2.38	77.65	2.24
13	69.56	1.93	74.81	1.90
17	76.98	1.52	86.37	1.52
22	80.56	1.23	87.88	1.21
28	84.44	0.99	90.18	0.91
37	86.86	0.82	92.59	0.84
Average lung residual Error (%)	2.34		2.48	

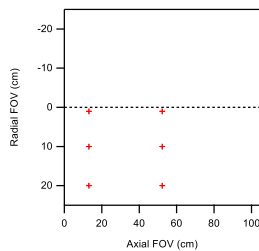
511

512 (B)

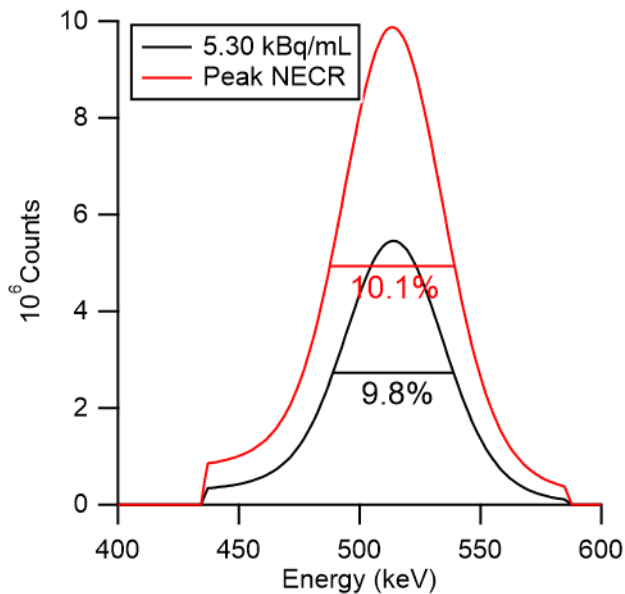
OSEM-TOF 4i5s	4 : 1 Sphere-to-background ratio		8 : 1 Sphere-to-background ratio	
	Contrast recovery (%)	Background variability (%)	Contrast recovery (%)	Background variability (%)
10	64.25	1.67	74.40	1.49
13	67.88	1.4	74.73	1.34
17	74.6	1.15	82.73	1.15
22	77.66	0.97	85.37	0.96
28	82.38	0.83	88.54	0.80
37	85.47	0.76	91.19	0.80
Average lung residual Error (%)	4.84		5.09	

513

514 **Supplemental Figures and Tables**



515
516 **SUPPLEMENTAL FIGURE 1:** Sagittal view of the FOV coordinates, with positions of the
517 point source for resolution measurements marked as red crosses.



518
519 **SUPPLEMENTAL FIGURE 2:** Sample histograms used for calculating energy resolution at
520 low activity concentration (black) and peak NECR activity concentration (red). The respective
521 FWHM's are given in percent of the peak energy

522 **SUPPLEMENTAL TABLE 1: Co-registration error measurements; maximal error***

@distance	Position	Co-registration error [mm]
5 cm	[0,1]	1.0
	[20,0]	0.98
	[0,20]	1.26
100 cm	[0,1]	1.08
	[20,0]	0.89
	[0,20]	1.38*

523

524

525

Graphical Abstract

